Materials Science in Semiconductor Processing 199 (2025) 109877

Contents lists available at ScienceDirect

Materials Science in Semiconductor Processing

journal homepage: www.elsevier.com/locate/mssp

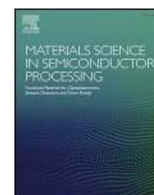

Influence of Al co-implantation on Ga distribution in *p*-type Ge

J. Perrin Toinin [a], A. Portavoce [b,*], M. Bertoglio [b], M. Descoins [c], M. Texier [c], D. Narducci [d], R. Daineche [c], K. Hoummada [c]

[a] *CEA Saclay, CEN Saclay, Gif Sur Yvette, 91190, France*
[b] *CNRS, IM2NP, Faculté des Sciences de Saint-Jérôme case 142, 13397, Marseille, France*
[c] *Aix-Marseille University, IM2NP, Faculté des Sciences de Saint-Jérôme case 142, 13397, Marseille, France*
[d] *Department of Materials Science, University of Milano-Bicocca, via R. Cozzi 55, 20125, Milano, Italy*

ARTICLE INFO

Keywords:
Germanium
Doping
Co-doping
Gallium
Aluminum

ABSTRACT

Pure Ge-based devices are of high interest for the development of complementary-metal-oxide-semiconductor (CMOS) technology in a wide range of applications, from standard microelectronics to more innovative applications such as CMOS photonics. However, the size reduction of Ge devices is limited by dopant activation. In this work, Ge *p*-type doping with Ga is studied in the presence of Al using conventional CMOS processes. Similar doses of Ga and Al ions were implanted or co-implanted in Ge (100) single crystals. Ga and Al atomic distributions were studied by secondary ion mass spectrometry, atom probe tomography, and transmission electron microscopy before and after rapid thermal annealing. Ga implantation leads to Ge amorphization and dislocation loops formation after subsequent recrystallization. These dislocation loops are shown to significantly limit the Ga doping level due to Ga segregation. Ge amorphization was not observed after Al implantation, and an entire Al dose of 3.5×10^{15} at cm^{-2} is fully soluble in Ge. However, Al activation is limited, suggesting that a large part of Al atoms occupies inactive interstitial sites. The presence of Al in Ga and Al co-implanted Ge is shown to prevent the formation of dislocation loops during annealing, and thus, to promote Ga full activation. This behavior is explained by the different diffusion mechanisms of Ga and Al in Ge. These observations suggest that a *p*-type doping level close to 1 at%, Ga solubility limit in Ge, could be reached in Ge by adjusting Al implantation conditions with CMOS doping process conditions.

1. Introduction

The performance and the applications of complementary-metal-oxide-semiconductor (CMOS) devices are governed by their size reduction. The miniaturization limit of 'standard' CMOS devices is constantly pushed back thanks to innovation, based on new component architectures (FINFET, FDSOI …) and alternative materials (Pt-rich NiSi contacts, high-k dielectrics …) [1,2]. The integration of pure Ge in CMOS technology in addition to Si and Si(Ge) opens new routes of development and innovations [3–5]. Ge possesses a smaller band gap and a higher charge carrier mobility, and allows lower process temperatures to be used compared to Si and Si(Ge) [6]. However, several potentially interesting Ge components need heavy doping such as for photodetection or for superconducting properties [7,8]. Furthermore, the ability to create highly doped *p/n* shallow junctions in Ge and to form stable ohmic contacts on doped-Ge are still currently the main obstacles slowing the development of Ge-based industrial technologies. In order to meet the constraints related to the fabrication of next-generation microelectronic devices (short-channel MOSFETs for example), the improvement of our knowledge on Ge doping and on ohmic contact formation on Ge using standard CMOS procedures is mandatory.

Ion implantation is commonly used to introduce dopants into semiconductors in CMOS technology. It allows the dopant profiles to be controlled in order to build thin junctions. Furthermore, co-doping was shown to increase dopant activation levels in Si and Ge, especially for *n*-type dopants [9–11]. However, ion implantation was shown to cause damage [12] and to induce partial amorphization of crystalline materials. In the case of silicon, the implantation-induced amorphous layer is recrystallized during annealing, but extensive defects may appear in the crystal close to the initial amorphous/crystal interface. In the case of germanium, in addition to amorphization [13], the material can be partially sputtered to form a porous honeycomb structure [14–23]. The investigation of sample morphology and the analysis of dopant redistribution in the implanted layers are therefore essential in order to

* Corresponding author.
E-mail address: alain.portavoce@im2np.fr (A. Portavoce).

https://doi.org/10.1016/j.mssp.2025.109877
Received 9 May 2025; Received in revised form 23 June 2025; Accepted 17 July 2025
Available online 19 July 2025
1369-8001/© 2025 The Authors. Published by Elsevier Ltd. This is an open access article under the CC BY license (http://creativecommons.org/licenses/by/4.0/).

achieve high-quality doping.

Herein we present a study on *p*-type Ge doping using standard CMOS doping processes consisting of two steps: i) implantation of *p*-type dopants in a low and uniformly doped *n*-type Ge single crystal substrate, followed by ii) thermal annealing aiming at both removing implantation defects and activating the dopants, ideally allowing all the implanted dopants to occupy substitutional sites in perfectly crystalline Ge. Ga and Al were chosen as *p*-type dopants, as they were expected to be among the best Ge dopants due to their very high solubility [24] and their relatively low diffusion coefficients (see Refs. [25–27] for Al and ref. [28–30] for Ga). Furthermore, Ga and Al are in phase separation, as well as with Ge (no Ga-Al, Ga-Ge, or Al-Ge compounds). However, their activation levels reported so far in the literature remain quite lower than their expected solubility [31–33]. The reasons for these low activities need to be investigated, as the understanding of the physical mechanisms involved in this reduced activation could allow higher doping levels to be reached with a suitable process. Furthermore, as same-type dopant co-implantation was shown to improve activation [34], Ge *p*-type doping using Ga and Al co-implantation was also investigated. The aim of this study is i) to characterize the effects of Ga and Al implantation on the structure of Ge substrates (surface and volume), ii) to investigate Ga and Al diffusion and co-diffusion during thermal annealing, and iii) to correlate dopant distribution with dopant activation.

2. Experiments

Six identical Ge (001) substrates were implanted with Ga or Al. One set of samples was implanted with a single dopant (Ga or Al) and one set with both dopants (Ga and Al). As usual in current CMOS technology, the implants were performed at room temperature (T) under a pressure (P) of 10^{-7} Torr, limiting dopant diffusion and minimizing impurity incorporation. The Ge substrates were *n*-type Ge (100) single crystals of ~10 cm diameter with a thickness of 480 μm, uniformly doped with Sb (1×10^{17} at cm^{-3}), exhibiting a resistivity comprised between 0.059 and 0.088 Ω cm. Two different implantation doses were used (Table 1), their energy and dose determined using SRIM simulations [35]. The obtained dopant profiles are Gaussian with a maximum concentration located ~60 nm below the substrate surface. The first one, labelled 'high-dose', allows a maximum concentration of 5×10^{20} at cm^{-3} to be reached, and the second one, labelled 'low-dose', allows a maximum concentration of 1×10^{19} at cm^{-3} to be reached. The high-dose implants allow Ge doping to be studied in the conditions corresponding to the fabrication of desired *p*/*n* junctions, as well as to study the solubility of the dopants in Ge, implantation-mediated defect formation, dopant-defect and dopant-dopant interactions. Ga and Al high-dose implantations were also performed in pre-amorphized Ge (001) substrates using Ge implantation (Table 1) in order to assess the benefits of Ge pre-amorphization on Ga and Al doping. Ga and Al low-dose implants aim at minimizing defect formation in order to investigate dopant diffusion in Ge close to intrinsic conditions, without additional interactions.

After implantation, the Ge substrates were cut into several pieces of 1×1 cm^2 and were capped with a 5 nm-thick SiO_2 layer deposited by plasma enhanced chemical vapor deposition (PECVD) at ambient temperature in order to prevent dopant diffusion and avoid dopant thermal desorption during annealing. The low-dose samples and one set of high-dose samples were annealed at $T = 600$ °C for 30 min (labelled R0)

Table 1
Energy and dose of ion implantations.

Element	Implantation energy (keV)	Dose (at cm^{-2})	
		Low-dose	High-dose
Ga	80	6×10^{13}	3.0×10^{15}
Al	35	7×10^{13}	3.5×10^{15}
Ge	150	1×10^{14}	

under vacuum ($P \sim 10^{-7}$ mbar) in a standard rapid thermal annealing (RTA) furnace. This annealing allows amorphized Ge to be fully recrystallized while limiting dopant diffusion. The dopant distributions obtained after this step were used as initial distributions for dopant diffusion investigations using subsequent annealing under vacuum either at $T = 650$ °C for 168 h (labelled R1) or at $T = 750$ °C for 3 h (labelled R2). A second set of high-dose samples was annealed at $T = 700$ °C for 30 min by RTA (labelled R3) for dopant activation measurements. All the samples that experienced a same type of annealing (R0, R1, R2, or R3) were annealed together at the same time in order to improve dopant distribution comparisons. Thermal annealing was performed under vacuum in order to prevent sample oxidation.

Atom probe tomography (APT) analysis was performed using a CAMECA LEAP 3000X-HR system. The APT samples were prepared by focus ion beam (FIB) in an FEI Helios 600 NanoLab setup using the standard procedure described in Ref. [36]. Prior to FIB sample preparation, the SiO_2 capping layer was removed by chemical etching (2 min in 5 w% HF solution) and covered by a 100 nm-thick Ni layer for protection during the FIB process. The measurements were performed in the laser mode at T ~20 K with a laser energy of 0.07 nJ, corresponding to $I^{2+}_{Ge}/I^{1+}_{Ge} = 10$, a laser pulse frequency of 100 kHz, and an average detection rate of 2 ions per 1000 laser pulses. Finally, the data were processed with the software IVAS 3.6.14. HR-TEM and HAADF-STEM analyses were performed using an FEI Titan 80–300 Cs-corrected microscope operating at 300 kV and equipped with a Gatan Model Ultra Scan 1000P charged-coupling device (CCD) camera and a Gatan Model 806 annular HAADF-STEM detector. STEM images were acquired using a camera length of 195 mm (collecting angle between 29.77 and 182.08 mrad). TEM samples were prepared by FIB, followed by mechanical dimpling and Ar^+ ion milling using a Gatan Parallel Ion Polishing System. Secondary ion mass spectrometry (SIMS) was used to determine the dopant concentration profiles in the Ge substrates using a CAMECA IMS 3F setup with a 3 keV O_2^+ ion beam for the high-dose samples and a CAMECA IMS 7F for low-dose samples with a 5 keV O_2^+ energy ions beam. The SIMS analyses were performed with an 100 nA primary ion beam with an incidence angle of approximately 45° rastered over an area of 250 × 250 μm^2. The maximum SIMS doping level error was estimated to be 6 %, while the maximum SIMS profile integration error was estimated to be 13 %. Electrical Hall Effect measurements were performed in the Van der Pauw geometry using a lab-made setup to measure the concentration of free carriers in the sample after activation.

3. Results and discussion

3.1. Ga and Al atomic distributions

Ion implantations in Ge substrates can lead to Ge amorphization as well as to the formation of pores on the Ge surface [37,38]. High-dose Ga implantation is the implant causing the most damages in the Ge substrate. Fig. 1 presents a cross-section HR-TEM image of the high Ga dose as-implanted sample. Ge is amorphized down to a depth ~100 nm from the surface. The Ge surface, as well as the amorphous/crystalline interface, are characterized by a significant roughness. The surface roughness, extending down to an average depth of 10 nm, is the result of implantation-induced pore formation. Fig. 2 shows scanning electron microscopy (SEM) images of the surface of several high-dose implanted samples corresponding to a single implant of Ga (Fig. 2a) or Al (Fig. 2b), or to Ga and Al co-implantation (Fig. 2c). Only Ga implantation causes pore formation on the Ge surface. Furthermore, the average lateral size of the pores is not modified by Al co-implantation. In contrast to high-dose implanted samples, none of the low-dose implanted samples exhibits pores on their surface, the surface remaining flat after implantation.

The amorphous layer and the pores observed for high-dose Ga implants can be overhauled by thermal annealing. Fig. 3 presents cross-section TEM images of the Ga high-dose implanted sample after

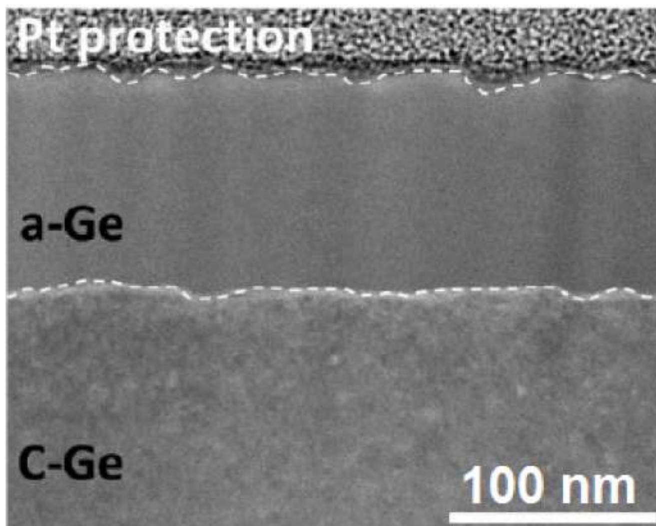

Fig. 1. Cross-section HR-TEM image of a high-dose Ga as-implanted sample.

annealing at 700 °C for 30 min (annealing R3). The Ge substrate is fully recrystallized. However, defects regularly distributed at a depth between 20 and 40 nm are observed (arrows in Fig. 3a). The nature of these defects was characterized in the same way as in Ref. [39], and are attributed to dislocation loops with an average lateral size ~ 3 nm. The dislocation density observed in Fig. 3a is $\sim 1.7 \times 10^{12}$ cm^{-2}. Considering that the thickness of the TEM lamella is ~100 nm, the dislocation loop density in the considered volume was estimated to be $\sim 1.7 \times 10^{17}$ cm^{-3}. STEM-HAADF images (Fig. 3b) show contrast variations in the recrystallized part of the Ge substrate. These contrast variations cannot be attributed to local chemical variations, as Ge and Ga atoms cannot be differentiated due to their very similar masses, but rather are attributed to structural defects in the Ge single crystal. The annealing R3 was chosen for Hall measurements for comparison with the literature data obtained with different dopants [32,33,40,41]. Similar structural properties with fewer dislocation loops were observed with the annealing R0 (RTP annealing at 600 °C for 30 min), associated with a strongly limited long-range atomic transport compared to the annealing R3 (average diffusion length >100 nm [42]). This annealing was chosen as the initial condition for Ga and Al diffusion investigations. Fig. 4 shows the SIMS profiles measured in the high-dose implanted samples either with Ga (Fig. 4a) or Al (Fig. 4b). After the annealing R0 (black empty triangles), the concentration profile is not significantly different from the implantation profile predicted by SRIM simulations (dashed black line). Concerning the Ga implanted sample (Fig. 4a), the diffusion profiles measured after annealing at 650 °C (R0 + R1) (blue empty circles) and 750 °C (R0 + R2) (red empty squares) show a first part of the profile below the surface corresponding to the thickness of the SiO_2 deposited by PECVD (Si profile plotted in gray dashed line). At the SiO_2/Ge interface (marked by a green dashed line) a concentration peak is detected. It corresponds to the matrix change between the Si oxide deposited on the surface and the substrate (matrix effect). In the same area, the Ge signal is also affected by a similar variation (not shown here). A discontinuity in the scattering profile forming a hump is observed at the depth corresponding to the maximum of the implantation peak (black arrow in the highlighted area), and corresponds to immobile Ga atoms. This effect is usually observed in SIMS profiles during the formation of precipitates. For both annealing, Ga clusters formed for concentrations above 1×10^{20} at cm^{-3}, although the Ga solubility limit (C_l) in Ge is higher than this value ($C_l = 3.4 \times 10^{20}$ at cm^{-3} at 750 °C and $C_l = 3.6 \times 10^{20}$ at cm^{-3} at 650 °C [24]) according to the literature. The Ga diffusion length found at a concentration of 1×10^{18} at cm^{-3} (classical junction depth) is 30 nm after the R0 annealing, considering the initial SRIM profile as reference. The diffusion lengths

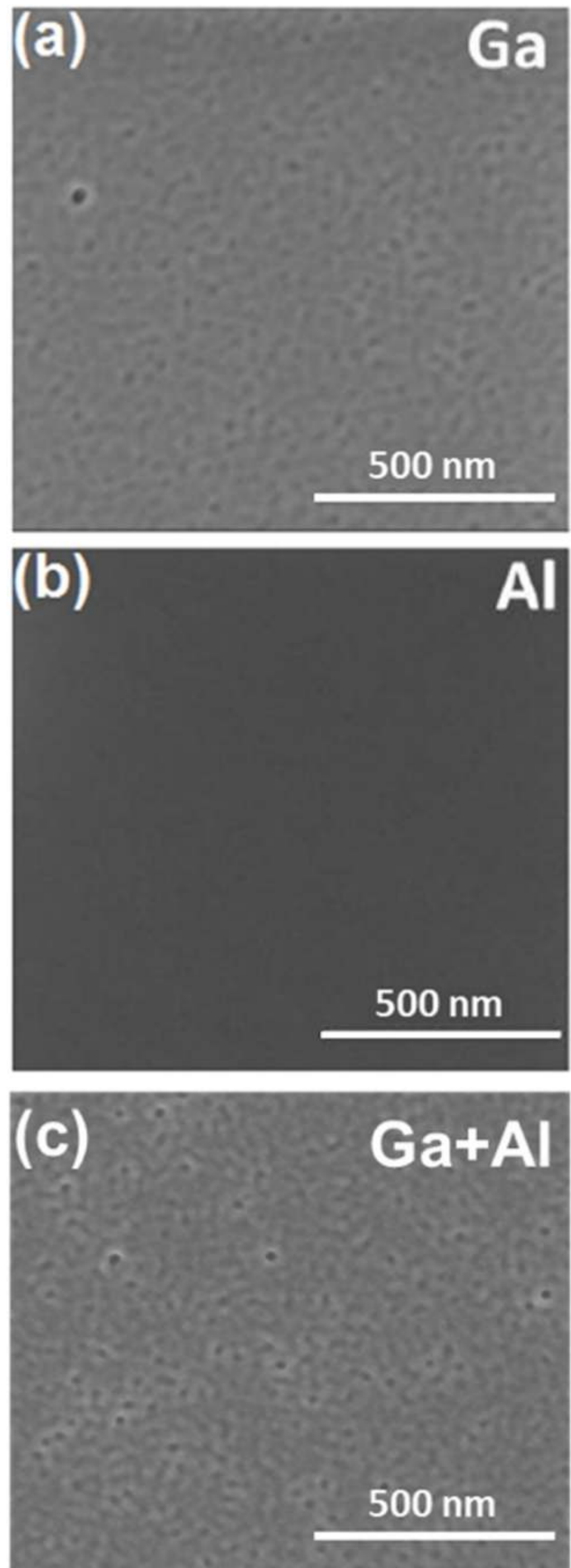

Fig. 2. SEM images of the high-dose implanted sample surface (implantation dose $\geq 3 \times 10^{15}$ at cm^{-2}): a) Ga; b) Al; c) Ga and Al.

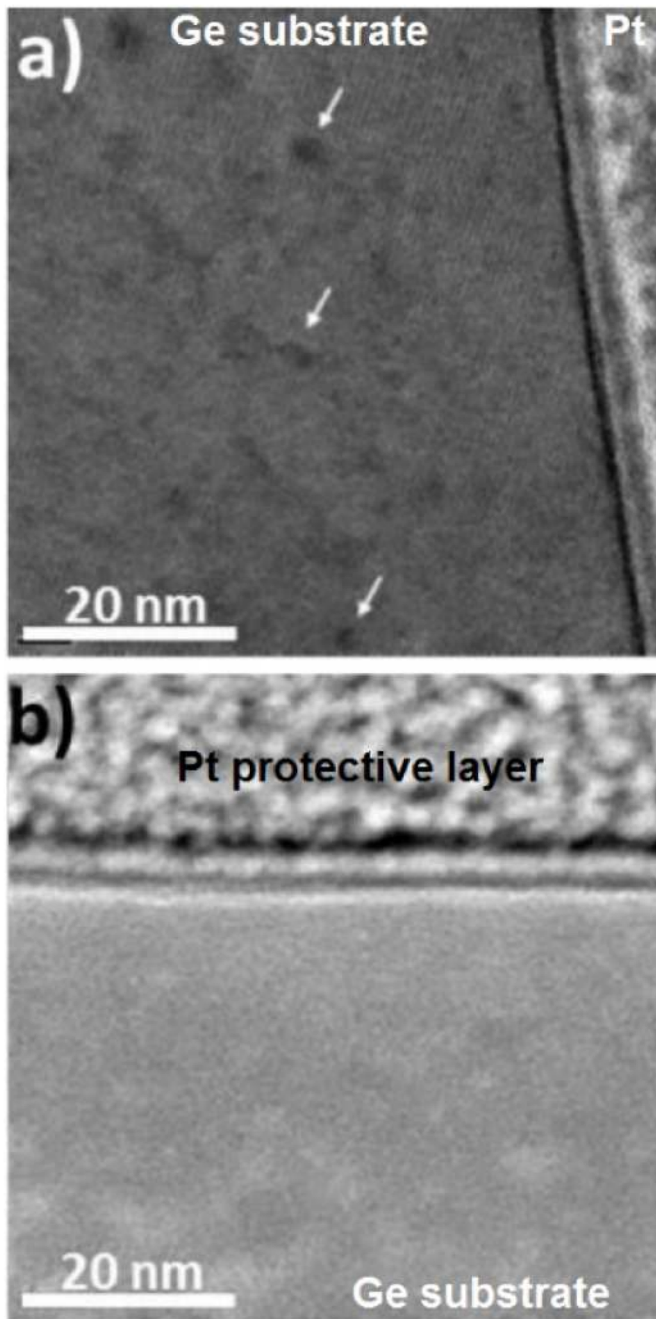

Fig. 3. TEM images of a Ge (100) substrate implanted with a high-dose of Ga and annealed at 700 °C for 30 min: a) image in HR-TEM mode, b) image in STEM-HAADF mode.

after R1 or R2 are almost identical with a junction depth ~220 nm. Note that the integrated dose on the profile beyond the SiO_2/Ge interface gives 2.2×10^{15} at cm^{-2} from the profile corresponding to R1 (650 °C) and 2.3×10^{15} at cm^{-2} from that corresponding to R2 (750 °C). These values are similar, confirming that the Ga dose stayed in the sample (no surface desorption) even though they correspond to a maximum dose loss of 27 %. Indeed, SIMS precision on integrated profiles is usually degraded by the atomic mixing [43] and the matrix [44] effects, especially when going through defects (interface, clusters, dislocation loops …). In our case, the dose variation observed by SIMS is likely due to the presence of Ga clusters in the samples annealed at 650 and 750 °C. Indeed, when analyzing high concentrations by SIMS, or because of a matrix effect between precipitates and a dilute solution, the ionization

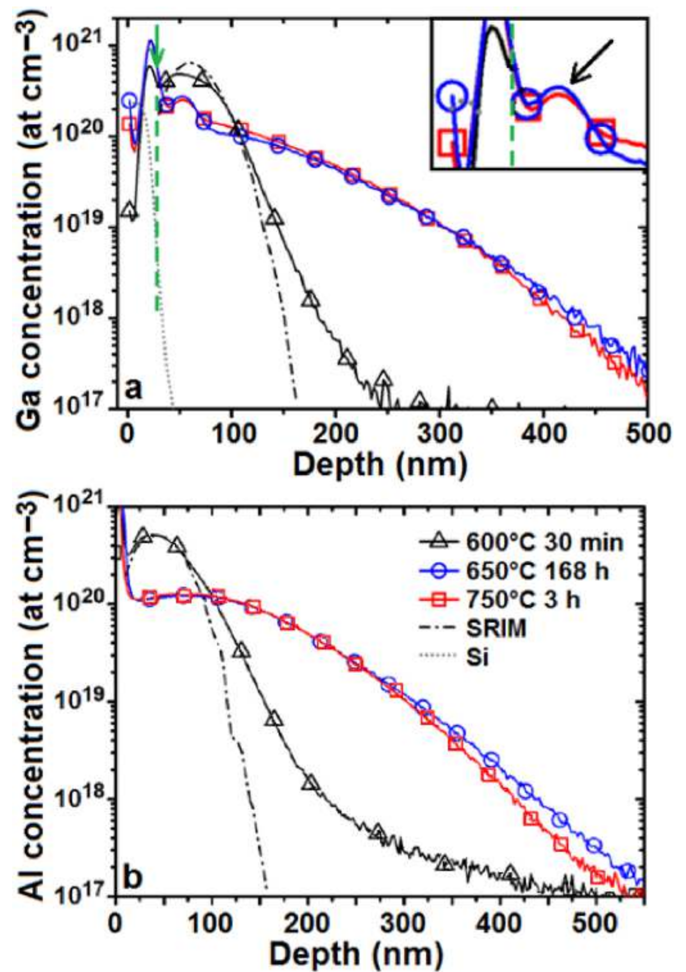

Fig. 4. SIMS measurements performed on high-dose implanted samples implanted either with Ga (a) or Al (b). The SIMS profiles were measured after the annealing R0 at 600 °C for 30 min (black empty triangles), as well as after the annealing R0 followed by a second annealing at 650 °C for 168 h (blue empty circles) or at 750 °C for 3 h (red empty squares). The dashed-dotted black profiles correspond to simulated implantation profiles using SRIM. The green arrow and the green dashed line show the interface between the SiO_2 cap and the Ge substrate.

rate may no longer be proportional to the concentration of the analyzed species, and thus the concentration in a high concentration region may be under- or over-estimated [44].

In the case of the sample implanted with a high dose of Al (Fig. 4b), the Al profile differs more strongly from the implantation profile predicted by SRIM simulations (dashed black line) than in the case of Ga after the annealing R0. Al diffused deeper than Ga, exhibiting a diffusion length ~50 nm at the concentration of 1×10^{18} at cm^{-3}. Furthermore, despite globally keeping a Gaussian shape after R0, the Al profile shows a second slope at its bottom (concentrations below 10^{18} at cm^{-3}) corresponding to an Al penetration down to a depth of ~500 nm before reaching the SIMS detection limit (i.e. 10^{17} at cm^{-3}). Fig. 4b shows that all implanted Al atoms diffused during both R1 and R2, suggesting that the Al solubility limit in Ge is higher than $\sim 5 \times 10^{20}$ at cm^{-2} in this temperature range. The Al solubility limit in Ge given in the literature [45] is $\sim 3.5 \times 10^{20}$ at cm^{-2} in this same temperature range. The diffusion lengths at a concentration of 1×10^{18} at cm^{-3} are 215 nm for annealing at 650 °C for 168 h and 200 nm for annealing at 750 °C for 3 h.

Fig. 5 presents APT measurements performed on the high-dose Ga implanted sample annealed at 650 °C (R0+R1). Fig. 5a shows an APT volume observed side view. Ga accumulations are detected in the APT

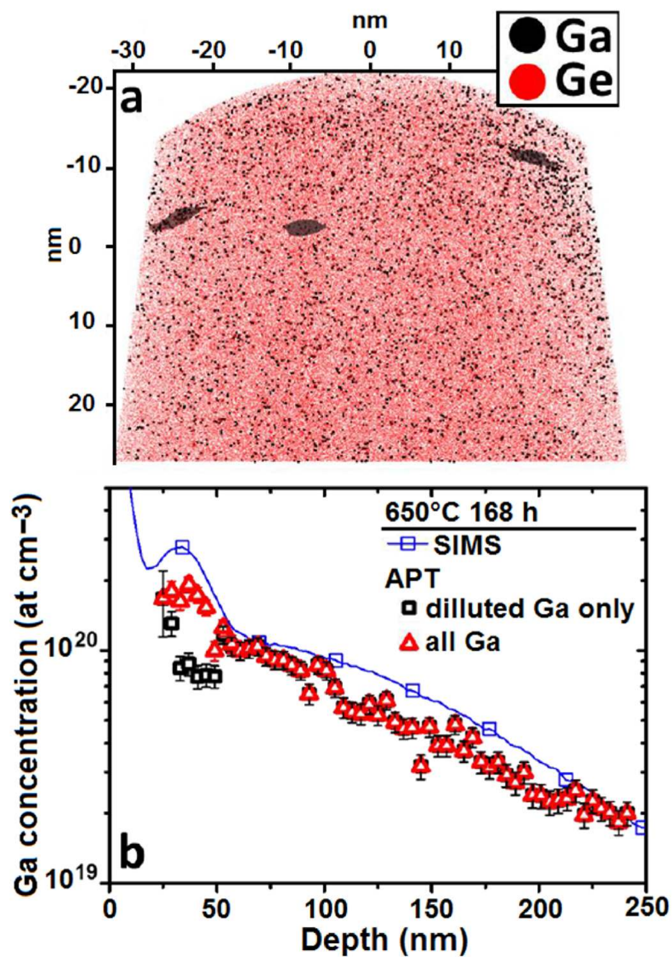

Fig. 5. APT measurements performed on the high-dose Ga implanted sample annealed at 650 °C for 168 h (R0+R1) compared to SIMS measurements performed on the same sample: a) cross-section view of an APT volume, each point is a single atom (red for Ge and black for Ga), and b) comparison between the SIMS profile (empty blue squares) and two APT concentration profiles corresponding to the entire Ga distribution (empty red triangles) or to Ga atoms in solution in Ge (empty black squares).

volumes. Each point is a single atom of Ge (red) or Ga (black) and Ga-rich accumulations are highlighted by 3 at% Ga black iso-concentration surfaces. These defects are localized in a 10 nm-wide region located at the implantation peak depth. Their density was estimated to be ~6×10^{16} cm^{-3} from several analyzed APT volumes. A statistical analysis of the detected Ga distribution using the IVAS cluster analysis tool revealed the presence of Ga-rich "clusters" at depths between 20 and 40 nm below the surface. The discrimination of Ga atoms in the clusters with respect to the rest of the matrix allowed the concentration profile of Ga atoms in solution in Ge to be obtained. Fig. 5b presents two concentration profiles measured in the same APT volume, corresponding either to the entire Ga distribution (red open triangles) or to the Ga atoms in solution in Ge (black open squares). The two profiles are compared to the SIMS profile (blue solid line and squares) measured in the same sample. The entire Ga distribution measured by APT is in good agreement with the SIMS profile. The differences observed between the two techniques can be attributed to a smaller statistic of APT measurements, sensitive to the sample inhomogeneity, and to the SIMS matrix effect in the cluster region located at the implantation peak [44]. The Gaussian-like distribution located at the implantation depth corresponds to immobile Ga atoms incorporated in disc-shaped Ga defects observed in APT volumes (Fig. 5a). In the defect vicinity, the proportion of Ga atoms in solution in Ge corresponds to 40 % of the total atoms and is lower than the concentration of Ga atoms in solution in neighboring regions without clusters (8×10^{19} at cm^{-3} versus 1×10^{20} at cm^{-3}). Deeper than the Ga defect region (below 50 nm), the SIMS profile corresponds to the diffusion profile of Ga atoms in solution in Ge. Fig. 6 presents the detailed analysis of the Ga accumulations observed in Fig. 5. Fig. 6a shows a 3D view of Ge, Ga, and Ni atoms distributed close to the three Ga-rich defects detected in the APT volume. Ni atoms come from the 100 nm-thick Ni cap that has been used to protect the sample before FIB sample preparation. As Ni occupies interstitial sites in Si and Ge, it can diffuse into Si and Ge at room temperature and segregate at defects such as dislocations and grains boundaries [39,46,47]. Fig. 6b and c respectively show the side view and the top view of one of the Ga-rich defects spotted in Fig. 6a (Ge atoms are represented by small red spheres, Ga atoms by large black spheres, and Ni atoms by green spheres). The defects correspond to planar defects and the presence of Ni atoms suggests a structural defect acting as a segregation site for interstitial Ni atoms. Fig. 6d shows the Ga concentration profiles in the two directions, parallel and perpendicular to the defect plane. On average, the defects are about 2 nm thick and 5 nm wide. Ga atoms have accumulated on 2 to 3 atomic planes (Fig. 6b). The angle between the horizontal axis of the APT volume (100 Ge plane) and the plane of the disk-shaped defect is 12° ± 5°, possibly corresponding to (105) or (116) Ge planes. The analysis of the Ge matrix atomic density in the defect vicinity shows no noticeable difference compared to the rest of the volume. This indicates that the defects with Ga accumulation have no impact on the tip evaporation during APT measurements, which generally corresponds to the case of solute atoms and not to that of clusters or precipitates (no local magnification or compression effect) [48].

Fig. 6e shows integrated concentration profiles [49] measured perpendicularly to the defect plane. The concentration difference between the integrated profile obtained in the matrix before and after passing through the defect allows the defect excess concentration (in at % nm) to be determined [49]. Knowing the defect thickness, one can deduce its Ga concentration. Considering the average defect thickness to be 2 nm, the Ga and Ni concentrations of the defect selected in Fig. 6 are 4.25 Ga at% and 0.6 Ni at%. The Ge-Ga binary phase diagram corresponds to phase separation without compound formation. As there are no intermediate phases between Ge and Ga, the only precipitates that could be observed are pure Ga precipitates. However, Ga-rich regions correspond to accumulations below 5 Ga at%, and these Ga-rich regions do not cause usual APT artifacts, leading to significant density variations near precipitates in APT reconstructed volumes [50]. Indeed, pure Ga precipitates are expected to display an evaporation field about twice as small as that of the Ge matrix [47] leading to significant density variations in Ge APT volumes [50]. The detection of Ni atoms only in the vicinity of Ga-rich areas is also significant. As already mentioned, the Ni source is the Ni layer deposited on the surface of the sample before FIB preparation in our case. Ni is known to diffuse on Ge interstitial sites at room temperature [51]. However, its solubility limit being very low in Ge, Ni can be detected in Ge by APT only on defects on which Ni segregates, exhibiting Ni concentrations well above its solubility limit. In particular, it has been shown by APT that Ni forms Cottrell atmospheres [46] around dislocation loops in Si and Ge [42,46]. The size of the dislocation loops observed by TEM (Fig. 3), as well as their shape, their depth location and their density are comparable to the size, shape, depth and density of the Ga-rich defects observed in APT volumes. These observations lead to the conclusion that Ga-rich defects decorated with Ni atoms observed in APT volumes do not correspond to Ga precipitates, but correspond to Ge dislocation loops formed during the annealing R0, decorated with co-segregated substitutional Ga atoms and interstitial Ni atoms. Consequently, the concentration limit determined by SIMS (Fig. 4), above which Ga atoms are found to be immobile, does not correspond to Ga solubility in Ge at the annealing temperature used for R1 and R2, but to Ga segregation on dislocation loops, explaining why this concentration limit is actually much lower than the Ga solubility

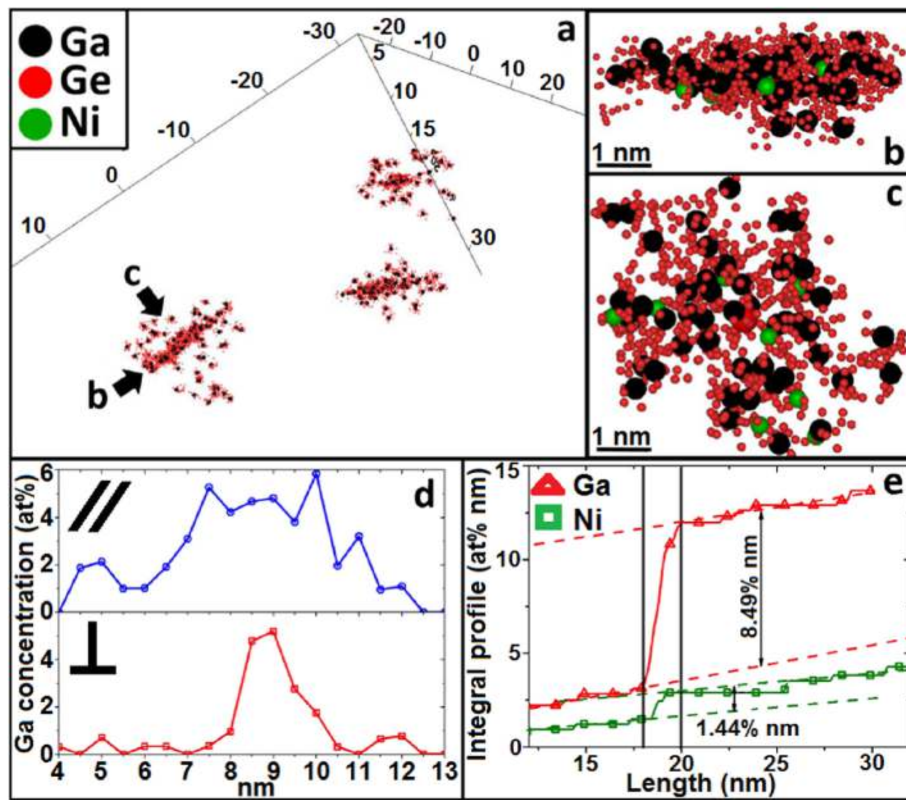

Fig. 6. APT analysis of Ga-rich defects: a) 3D view of the Ga-rich defects in the APT volume, only the atoms considered to belong to the defects are shown (red Ge atoms, black Ga atoms and green Ni atoms); b) cross-section view of a single defect from (a); c) top view of the same single defect from (a); d) concentration profile across the same defect (red squares profile perpendicular to the defect plane, blue squares profile parallel to the defect plane, see arrows in fig (a)); e) Ga (red triangles) and Ni (green squares) integrated profiles determined perpendicularly to the defect plane.

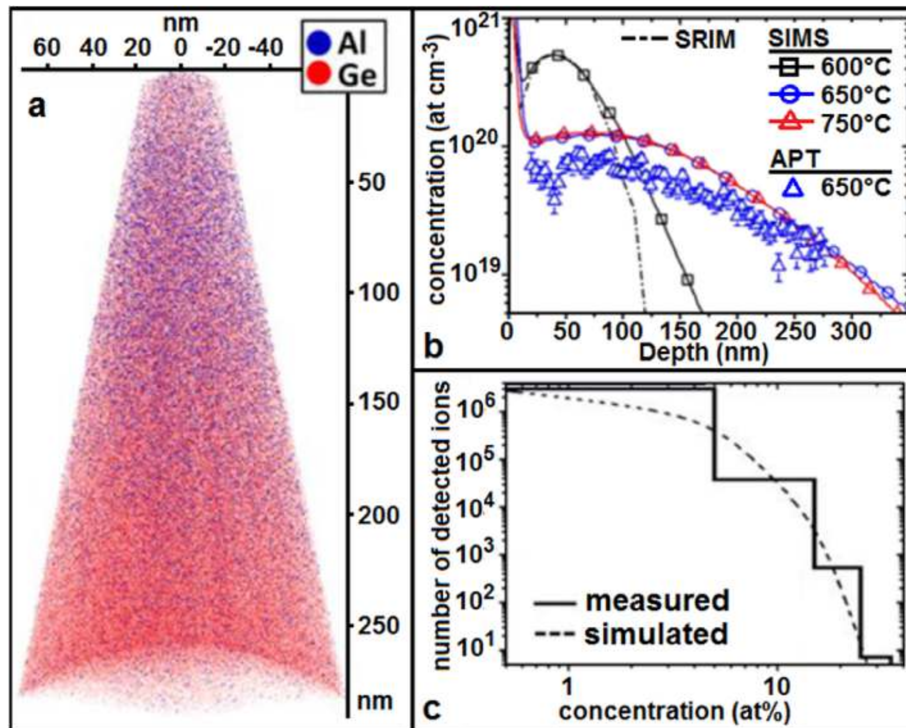

Fig. 7. APT measurements performed on the high-dose Al implanted sample annealed at 650 °C for 168 h (R0+R1) compared to SIMS measurements performed on the same sample: a) side view of an APT volume, each point is a single atom (red for Ge, and blue for Al); b) comparison between the Al concentration profiles determined by APT in the volume (empty blue triangles) shown in (a) and the profile measured by SIMS (solid lines); and c) comparison between the Al atom distribution determined by APT (solid line) in the volume shown in (a) and a binomial random distribution.

limit in Ge.

Fig. 7 presents APT and SIMS measurements performed on the high-dose Al implanted sample annealed at 650 °C (R0+R1). Al clusters or Al accumulations are not observed in APT volumes (Fig. 7a). Furthermore, the Al concentration profile measured by APT is in agreement with that obtained by SIMS (Fig. 7b). Fig. 7c shows a comparison between the Al distribution determined by APT and a simulated binomial random distribution corresponding to the same amount of Al in logarithmic scale. The good agreement between the two distributions confirms that Al atoms are randomly distributed in Ge, corresponding to solute Al atoms in agreement with the SIMS profiles (Fig. 7b), showing fully mobile Al atoms for the two annealing R1 (650 °C) and R2 (750 °C). These observations suggest that the Al solubility limit in Ge is greater than 5×10^{20} at cm^{-3}, which is higher than that generally considered in the literature (i.e. 3.1×10^{20} at cm^{-3} at 650 °C and 3×10^{20} at cm^{-3} at 750 °C [42]).

Ga and Al co-implanted samples were prepared by sequential implantation of first Ga and second Al. The implantation conditions were identical to those used for the samples implanted with a single element (Ga or Al). Furthermore, the co-implanted samples were simultaneously annealed with the samples implanted with a single element for reliable comparisons. Fig. 8 presents the comparison between Ga (Fig. 8a) and Al (Fig. 8b) concentration profiles measured by SIMS in the different samples containing either a single element (Ga or Al, solid symbols) or containing both elements (Ga and Al, open symbols). Contrasting with the sample only implanted with Ga, Ga SIMS profiles measured in the Ga and Al co-implanted sample after the annealing R1 and R2 do not evidence any Ga clusters or Ga segregation on dislocation loops (see inset in Fig. 8a), since the entire Ga dose is found to be mobile. Furthermore, the Ga diffusion depth is similar in the two samples with or without Al, suggesting that Ga diffusion is not significantly modified by the presence of Al atoms. In the case of Al (Fig. 8b), the totality of Al atoms remains mobile during annealing in the presence of Ga, but the Ga implant causes a more noticeable effect on Al diffusion kinetics. Indeed, the presence of Ga leads to an increase of Al diffusion kinetics. Al diffusion depth in the Ga and Al co-implanted sample after either annealing R1 or R2 is at least 40 nm deeper than in the sample without Ga at the concentration of 1×10^{18} at cm^{-3}. The Al concentration close to the sample surface is also lower in the co-implanted sample (i.e. 7×10^{19} at cm^{-3}) than in the sample only implanted with Al (i.e. 1×10^{20} at cm^{-3}). Fig. 9 presents the APT measurements performed on the high-dose Ga and Al co-implanted sample after annealing at 650 °C (R0+R1) compared to the SIMS measurements performed on the same sample. Contrasting with the sample only implanted with Ga (Fig. 5), all the Ga atoms are found randomly distributed in the volume (Fig. 9a). Neither Ga segregation nor Ni segregation can be detected in the sample containing Al. Similar to the case of a single Al implant (Fig. 7), Al atoms are also found to be randomly distributed in presence of Ga (Fig. 9a). Fig. 9b shows that the SIMS profiles are in good agreement with the APT profiles measured in the volume presented in Fig. 9a.

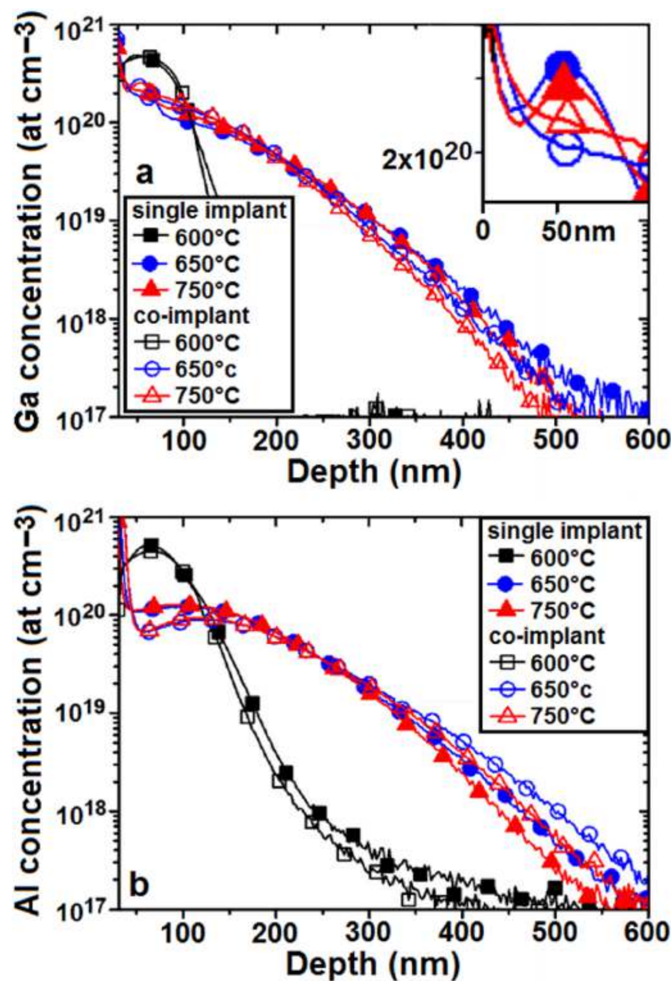

Fig. 8. Comparison between Ga and Al SIMS profiles measured after same annealing in samples implanted either with a high dose of a single element (Ga or Al, solid symbols) or with the same high doses of the two elements (Ga and Al, open symbols): a) Ga profiles, and b) Al profiles.

3.2. Ga and Al diffusion

Fig. 10 presents the Ga SIMS profiles measured in the Ge sample implanted with a low dose of Ga after the annealing R0+R1 (blue open circles) and R0+R2 (red open triangles), compared to the Ga SIMS profiles measured in the same sample after the annealing R0 (black open

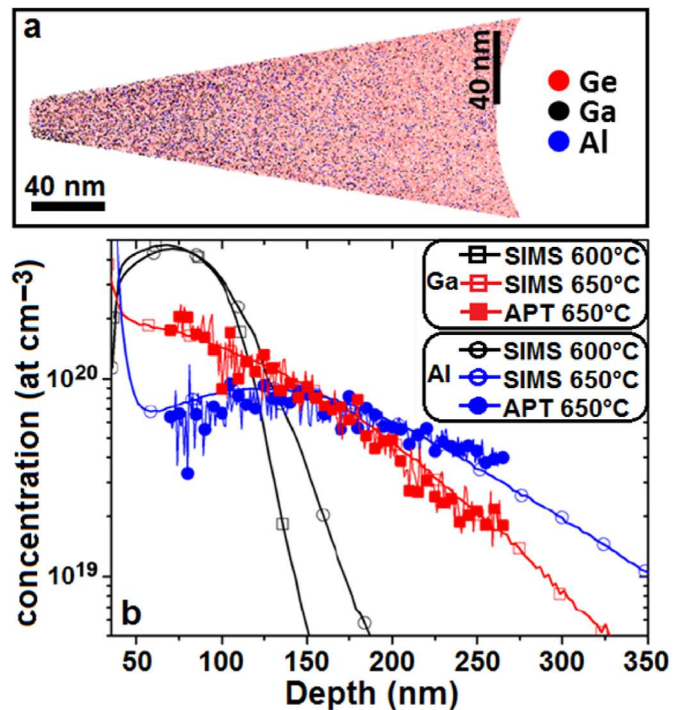

Fig. 9. APT measurements performed on the high-dose Ga and Al co-implanted sample annealed at 650 °C for 168 h (R0+R1) compared to SIMS measurements performed on the same sample: a) cross-section view of an APT volume, each point is a single atom (red for Ge, black for Ga, and blue for Al); and b) comparison between the SIMS profiles (open symbols) and the APT concentration profiles (solid symbols) of Ga (squares) and Al (circles) measured in the volume presented in (a).

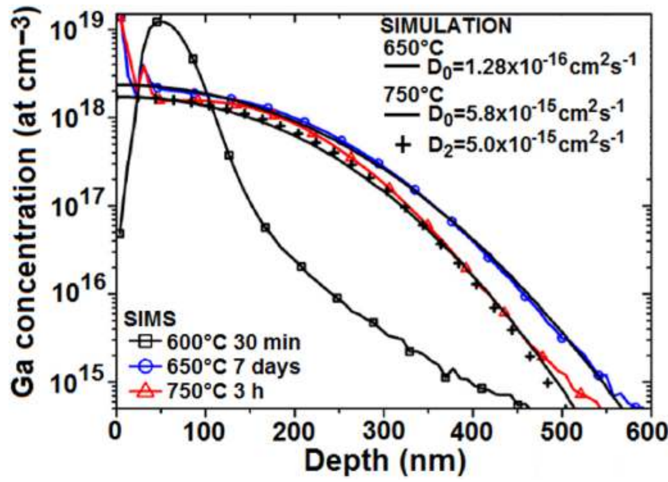

Fig. 10. Comparison between experimental and simulated Ga concentration profiles. Simulations consider the SIMS profile measured after the annealing R0 (600 °C for 30 min) as initial dopant distribution.

squares). All the Ga atoms are mobile for this implantation dose. The diffusion lengths are very similar to those measured in the high-dose implanted samples (Fig. 4). These profiles were simulated using a modified Fick diffusion equation, considering the profile measured after R0 as the initial distribution. Indeed, the formation of an internal electric field resulting from the variation of the fermi level with the local dopant concentration in the material must be considered in the diffusion flux J [52]:

$$J = -D\left(\frac{n}{n_i}\right)^{-q}\frac{\partial}{\partial x}\left(C\left(\frac{n}{n_i}\right)^{+q}\right) \quad \text{Eq. 1}$$

D is the effective diffusion coefficient of the dopant, q is the charge of the dopant when activated, n is the local free electron concentration and n_i is the intrinsic free electron concentration in the material at the considered temperature. Furthermore, the coefficient D must consider the contribution of charged point defects, for which the concentration can vary with the Fermi level in the material, leading to a dopant effective diffusion coefficient depending on the dopant concentration. In this case, the effective diffusion coefficient of a p-type dopant, such as Ga, can be expressed as [53]:

$$D = D_0 + D_1\left(\frac{p}{n_i}\right) + D_2\left(\frac{p}{n_i}\right)^2 \quad \text{Eq. 2}$$

D_0 is the diffusion coefficient related to mobile species (dopant-vacancy pairs for example) whose concentration is independent of the hole concentration p, which are often uncharged. D_1 is the diffusion coefficient related to mobile species whose concentration is proportional to the hole concentration, and may possess a single positive charge. Finally, D_2 is the diffusion coefficient related to mobile species whose concentration depends on the square of the hole concentration, and may possess two positive charges. One should note that eq. (2), taking into account the variation of point-defect concentrations with Fermi level variations through coefficients D_1 and D_2, leads to abrupt diffusion profiles different from Fickian profiles, sometimes referred to “box-like” diffusion profiles, such as the profile shown in Fig. 11a with open up-triangles. In our case, we considered that the hole concentration p is equal to the dopant concentration, considering that all the dopants are active. Ga atoms are simple acceptors corresponding to $q = 1$ and $n_i = 3.4 \times 10^{18}$ cm^{-3} at $T = 650$ °C and $n_i = 6.4 \times 10^{18}$ cm^{-3} at $T = 750$ °C in Ge [54] with $n \times p = n_i^2$. The maximum ratio in our samples is $p/n_i \sim 3$ at 650 °C and $p/n_i \sim 1.5$ at 750 °C at the beginning of annealing, for example.

Several simulations were performed combining eqs. (1) and (2), aiming at fitting experimental Ga profiles. In the case of Ga profiles measured in the Al-free sample, the best fit of the SIMS profile measured after annealing at 650 °C is obtained for $D = D_0 = 1.28 \times 10^{-16}$ cm^2 s^{-1} and $D_1 = D_2 = 0$ (solid line on R0+R1 profile in Fig. 10). The diffusion coefficient is independent of the doping level in this case. A satisfactory fit of the SIMS profile measured after annealing at 750 °C is also obtained considering the diffusion coefficient to be independent of Ga concentration with $D_0 = 5.8 \times 10^{-15}$ cm^2 s^{-1} and $D_1 = D_2 = 0$ (solid line on R0+R2 profile in Fig. 10). However, a better fit is obtained at 750 °C considering the contribution of charged species. Indeed, the best fit of the SIMS profile measured after annealing at 750 °C is obtained with $D_2 = 5.0 \times 10^{-15}$ cm^2 s^{-1} and $D_0 = D_1 = 0$ (black crosses in Fig. 10). Ga diffusion should be mediated by point defects exhibiting a concentration proportional to the square of Ga^- concentration in this case. One should note that the redistribution of the entire part of mobile Ga atoms can be simulated with eqs. (1) and (2), meaning that point defects mediating Ga diffusion are at equilibrium during annealing, as assumed by these two equations.

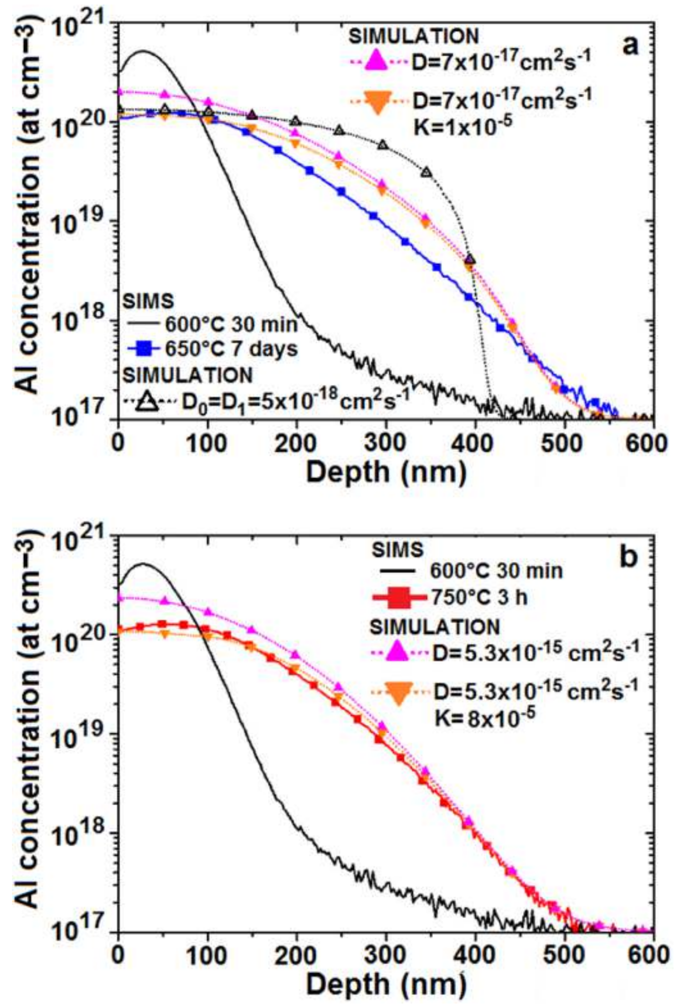

Fig. 11. Comparison between experimental and simulated Al concentration profiles. Simulations consider the SIMS profile measured after the annealing R0 (600 °C for 30 min) as initial dopant distribution.

Al is also a single acceptor p-type dopant of Ge, and because the entire Al dose is mobile for both low-dose implantation and high-dose implantation, Al SIMS profiles for both cases are expected to be fit using the same equations as for the low-dose Ga implantation case. Fig. 11a and b shows the measured and simulated Al profiles after the annealing R0+R1 (Fig. 11a) or R0+R2 (Fig. 11b). Al SIMS profiles cannot be fit using the same model as used for Ga. Charged point defects

show no contribution to Al diffusion in Ge ($D_1 = D_2 = 0$ in eq. (2)). Charged point defects having their concentration varying with activated Al atoms would favor the formation of box-like diffusion profiles, very steep at the end of the profile, such as the simulated diffusion profile shown in Fig. 11a with open up-triangles for example ($D_0 = D_1 = 5 \times 10^{18}$ cm^2 s^{-1} and $D_2 = 0$), increasing discrepancy between experiments and simulations. Furthermore, Al SIMS profiles cannot be fit by the classical Fickian diffusion model with constant D as shown in Fig. 11a (solid up-triangles) and 11b (solid up-triangles), considering $D = D_0$ and $D_1 = D_2 = 0$. Indeed, depending on the chosen coefficient, the obtained simulated profiles overestimate either the concentration close to the surface (solid up-triangles in Fig. 11a and b) or the diffusion length in the volume (not shown).

Simulations suggest that a part of the Al atoms is missing in the SIMS profiles (no dose conservation). In order to consider a possible dose variation, a second model allowing the Al dose to be reduced at the SiO_2/Ge interface was considered. In this model, a reaction driving force ($0 <$ coefficient $k < 1$) is considered at the SiO_2/Ge interface, which could be attributed to Al desorption from the SiO_2 surface or to Al reaction with the SiO_2 layer for example. Indeed, it has been shown that Al displays a strong reactivity with oxygen to form Al_2O_3, and this even in the case of a deep implantation in Ge [27] or Si [55]. Furthermore, Ellingham's diagrams show that Al_2O_3 is more stable than SiO_2, supporting the growth of Al_2O_3 while consuming SiO_2. The diffusion equation contains an additional term in this case:

$$\frac{\partial C(x,t)}{\partial t} = -\frac{\partial J}{\partial x} - kC(x \to 0) \qquad \text{Eq. 3}$$

This model still does not allow adequate simulation of experimental Al profiles. Increasing k allows the experimental profile in volume to be better reproduced, but the surface concentration is then too low compared to the experimental profile (not shown). In contrast, adjusting k aiming at reproducing the experimental profile close to the surface, leads to overestimating the concentration in volume (simulated profiles presented in Fig. 11a and b with down solid triangles). These observations suggest that Al atoms neither use the same dopant-vacancy pair mechanism as most dopants in Ge, such as p-type Ga and Mn atoms and n-type P, As, and Sb atoms, nor use a simple Fickian-type mechanism with a constant diffusion coefficient.

Fig. 12a shows the Ga SIMS profiles measured in the Ge (001) substrate implanted with the single low-dose of Ga and that measured in the Ge (001) substrate implanted with both the Ga and Al low-doses after same annealing. All Ga profiles measured after the annealing R0, R0+R1, and R0+R2 in the two samples with or without Al are similar. Comparable to the high-dose implants (Fig. 8a), Ga diffusion kinetic is not affected by Al co-diffusion. Furthermore, the Ga diffusion coefficients determined at 650 °C and 750 °C (Fig. 10) are in good agreement with the literature, corresponding to a vacancy-mediated mechanism [28,29,56]. Fig. 12b presents Al SIMS profiles measured in the Ge (001) substrate implanted with the Al low dose. The concentration profile measured after the annealing R0 (600 °C for 30 min, black solid squares) displays a maximum close to the surface (i.e. SiO_2/Ge interface), exhibiting an Al concentration higher than that of the initial Al distribution before annealing, initially located at a depth of ~60 nm. Furthermore, the profile is no longer Gaussian, displaying a first quasi-linear part from the surface down to a depth of ~150 nm and a second part with a different slope between a depth of 150 nm and 250 nm. After the annealing R0+R1 and R0+R2, the profile maximum remains localized at the Ge surface and the Al diffusion profiles are quasi-linear. However, one can observe the beginning of a hump close to a concentration of ~10^{18} at cm^{-3} in the Al profile measured after the annealing R0+R2. The two profiles end with a concentration plateau between 2×10^{15} and 1×10^{16} at cm^{-3}. These diffusion profiles are unusual and cannot be simulated using eqs. (1)–(3). They suggest more complex diffusion mechanisms, such as the case of W in Si for example [57].

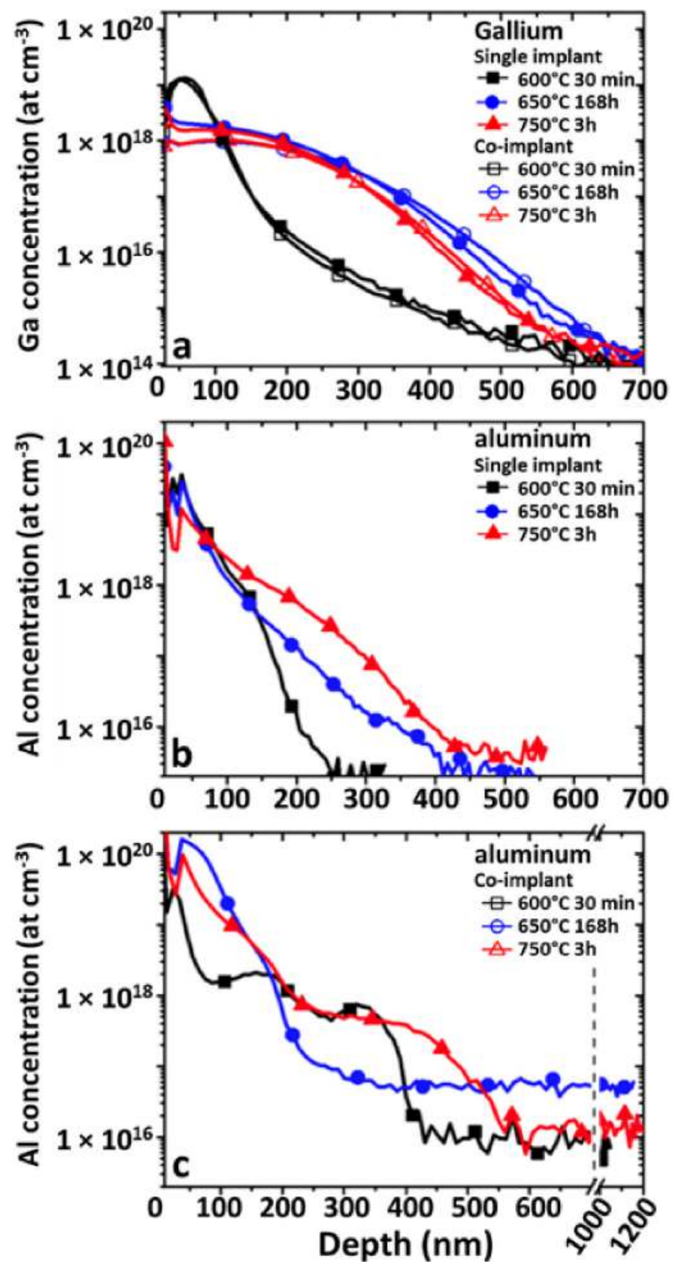

Fig. 12. Comparison between Ga or Al SIMS profiles measured in low-dose implanted samples after same annealing either in the sample implanted with a single dopant or in the sample co-implanted with the two dopants: a) Ga profiles, b) Al profiles measured in the sample implanted with Al only, and c) Al profiles measured in the sample implanted with Al and Ga.

Fig. 12c presents the Al co-diffusion profiles with Ga. These profiles are significantly different from that of Al diffusion without Ga (Fig. 12b). The Al concentration maximum has shifted towards the Ge surface as in the Ga-free samples, but concentration plateau are observed in the Al concentration profiles for all annealing. Furthermore, the Al penetration in Ge is unexpectedly deep below 10^{18} at cm^{-3}, larger than 1 μm for the annealing R0+R1 and R0+R2. These observations suggest that the "missing" part of the Al dose in the Al SIMS profiles measured in the high-dose samples (Fig. 11a and b) is the result of fast Al diffusion at low concentration levels. This phenomenon was already observed in the profile measured after pre-annealing (annealing R0) in Fig. 11a and b, with a maximum penetration depth of ~200 nm for concentrations above 10^{18} at cm^{-3} and a maximum penetration depth of ~500 nm for concentrations below 10^{18} at cm^{-3}. Al diffusion mechanisms seem to be

identical with or without Ga implantation. Indeed, a shift of the maximum Al concentration towards the sample surface is observed in the two cases. Furthermore, the hump and the plateau at the end of the Al profile measured in the sample without Ga (solid triangles in Fig. 12b) after the annealing R0+R2 appear to correspond to the same phenomenon observed in the sample implanted with Ga (solid triangles in Fig. 12c) and annealed in the same conditions, Ga allowing this phenomenon to be significantly enhanced. This suggests that the Al diffusion mechanism is not modified by Ga, but that the concentration of the point defect mediating Al diffusion is significantly higher in the sample implanted with Ga. It is worth noting that the hump formed in the Al profiles (Fig. 12c) cannot be attributed to an effect of charged defect concentration variations due to the variation of the Fermi level in the sample (box-like profiles such as the simulated profile presented in Fig. 11a, open up-triangles), since $p/n_i \sim 1$ in the samples implanted with the low Ga and Al doses at the considered annealing temperatures.

Diffusion kinetic of a given element in a given matrix is proportional to the concentration of the point defect involved in the diffusion mechanism. Since Ga diffusion is not disturbed by Al diffusion, but Al diffusion is modified by the presence of Ga, the point defect involved in the Al diffusion mechanism is not vacancy, and its concentration is increased by Ga implantation. Contrasting with Al implantation, Ga implantation was shown to lead to severe alteration of the Ge atomic lattice, leading to Ge surface sputtering (Fig. 1), Ge amorphization (Fig. 2) and to dislocation loop formation (Fig. 3). Dislocation loop formation in ion-implanted Si and Ge generally results from self-interstitial coalescence [58–60], which is the point defect in highest concentration in Si and Ge after ion implantation [60]. Since SIMS and APT measurements show the presence of dislocation loops in Ge implanted with Ga, but not in Ge co-implanted with Ga and Al (Figs. 4, 5 and 7), our results lead to the conclusion that Al diffusion is mediated by Ge self-interstitials. Ga implantation leads to a significant concentration of Ge self-interstitials, promoting the formation of dislocation loops without Al, decreasing the concentration of Ga atoms in solution due to Ga segregation on the dislocation loops. Al implantation does not lead to a large concentration of self-interstitials, but Al diffusion being mediated

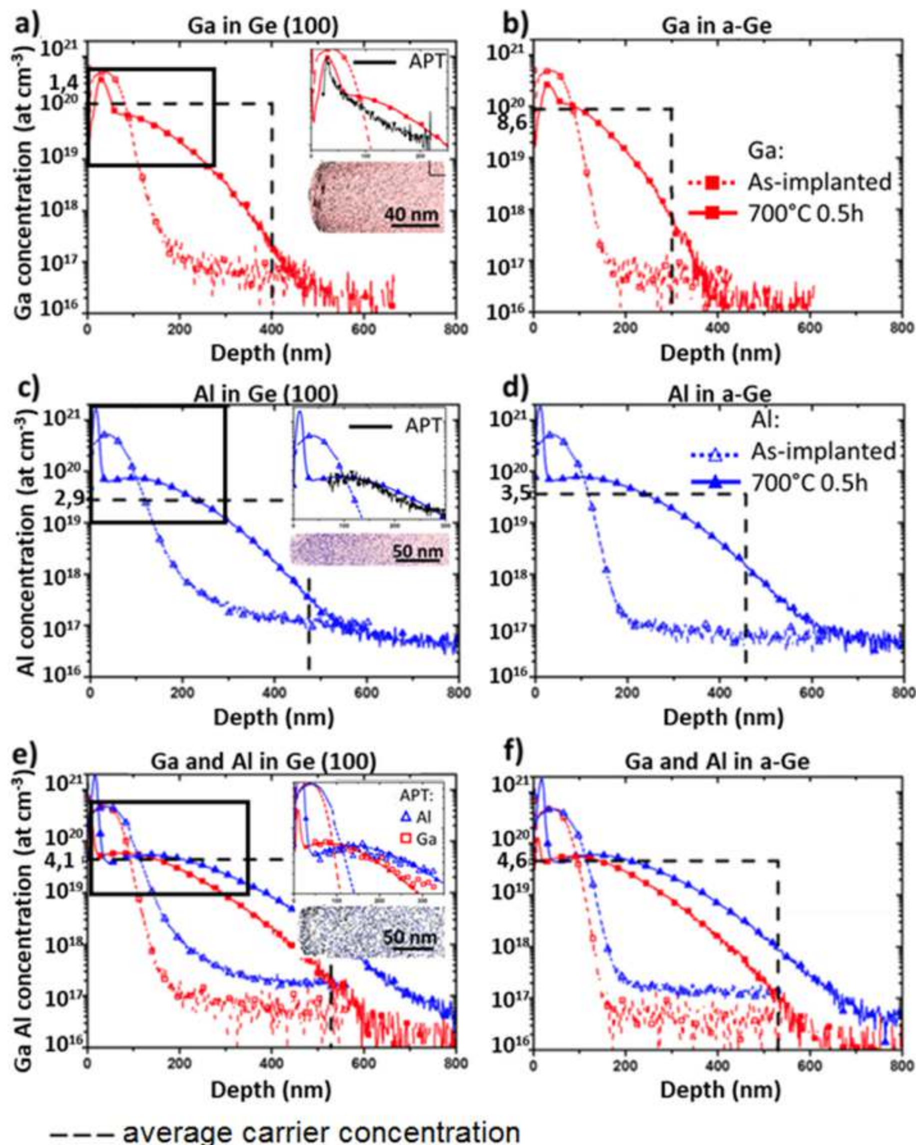

Fig. 13. SIMS and APT profiles measured before and after annealing at 700 °C for 30 min (annealing R3). The horizontal dashed line corresponds to the average free carrier concentration measured by HE considering the dopant penetration depth indicated by the vertical dashed line. a) single high-dose Ga implantation in Ge (001), b) single high-dose Ga implantation in pre-amorphized Ge (001), c) single high-dose Al implantation in Ge (001), d) single high-dose Al implantation in pre-amorphized Ge (001), e) high-dose Ga and Al co-implantation in Ge (001), and f) high-dose Ga and Al co-implantation in pre-amorphized Ge (001). APT analyses are displayed as insets in the corresponding SIMS figures (black dots for Ga atoms, blue dots for Al atoms, and red dots for Ge atoms).

by Ge self-interstitials, Al diffusion prevents the formation of dislocation loops by self-interstitial coalescence and is significantly enhanced in the sample co-implanted with Ga.

3.3. Ga and Al doping

Dopant activation in Ge was studied in six different samples in order to complement structural and chemical analyses, and also to determine the most-promising doping process between single high-dose Ga or Al implantation, and Ga and Al co-implantation either in crystalline Ge (001), or in pre-amorphized Ge (001) using Ge implantation (a-Ge) (Table 1) and the annealing R3. Dopant distributions in these samples were investigated using SIMS and APT measurements. The average activation level in each sample was determined using electrical Hall Effect (HE) measurements. Contrasting with previous samples, these samples were directly annealed at 700 °C for 30 min (i.e. annealing R3) after implantation, without the pre-annealing R0. Therefore, additional non-equilibrium phenomena are expected to occur in these samples during annealing, such as a transient acceleration of atomic diffusion (Transient Enhanced Diffusion [61]) for example. Average free carrier concentrations were determined in each sample (horizontal dashed line in Fig. 13) from HE measurements considering that the probed thickness corresponds to the penetration depth of the dopant measured after annealing in the SIMS profiles. This depth was considered to be the depth at which dopant concentration has decreased by two decades compared to its maximum concentration (vertical dashed line in Fig. 13). The contribution of Ge substrate intrinsic doping (*n*-type) on HE measurements is negligible. The maximum error on doping levels determined from HE measurements was estimated to be 12 %.

The average doping level reached in each sample is compared to dopant distributions measured by SIMS and APT before and after annealing in Fig. 13. The sample exhibiting the highest doping level corresponds to the case of the single Ga implant performed in the Ge single crystal, with a carrier concentration of 1.4×10^{20} cm^{-3} (Fig. 13a). Such a doping level in Ge was already reported in the literature using similar Ga implantations [33]. This is significantly lower than 3.5×10^{21} cm^{-3}, the expected Ga solubility in Ge between 600 and 750 °C. The doping level obtained with the same Ga implantation in pre-amorphized Ge is slightly lower (8.6×10^{19} cm^{-3}), but in this case, Ge recrystallization led to a reduction of the *p/n* junction depth (i.e. of the Ga diffusion length) of about ~100 nm (Fig. 13a and b). In both cases (without and with Ge pre-amorphization), the Ga activation levels are close to the maximum concentrations of mobile Ga atoms determined by SIMS in the two samples. The APT measurements (insets in Fig. 13a) are in good agreement with the SIMS measurements, showing again that immobile and inactive Ga atoms are Ga atoms segregated on dislocation loops.

Al is known to possess a large solubility in Ge (~4×10^{21} cm^{-3} for $600 \leq T \leq 750$ °C), and Al implantation causes the formation of a minimum of defects in the Ge matrix (light element and low implantation energy). This explain why all the Al atoms, reaching a maximum concentration of 5×10^{20} cm^{-3} after implantation (Fig. 13c), are found to be mobile during annealing, showing no signs of Al cluster formation (Fig. 13c and d). The APT measurements are in good agreement with the SIMS measurements (insets in Fig. 13c), showing a full solubility of Al atoms in Ge (no Al clusters and no decorated defects detected). However, the concentration of active Al atoms is three times lower than the Al maximum concentration in the SIMS profile, suggesting that a non-negligible part of Al occupies non-active sites of the Ge lattice. Ge pre-amorphization has little influence on the concentration of active Al atoms (~3×10^{19} at cm^{-3} in both cases), as well as on Al diffusion. However, contrasting with Ga, one can note that Ge recrystallization tends to increase the *p/n* junction depth (~50 nm) rather than to reduce it. This opposite behavior of Ga and Al diffusion during Ge crystallization confirms again that the diffusion of these two elements in Ge use different point defects, suggesting that Ge crystallization temporarily reduces vacancy concentration and increases self-interstitial concentration.

Ga and Al co-implantation combined with the annealing R3 did not allow higher doping levels to be obtained (Fig. 13e and f). Without pre-annealing (annealing R0), Al and Ga diffusion are found to be enhanced when the two elements are co-implanted. Therefore, Ga and Al co-implantation leads to flatter and deeper concentration profiles under the same annealing conditions. The APT measurements are in good agreement with the SIMS measurements (insets in Fig. 13e), all the Ga and Al atoms are found to be in solution in Ge, and clusters and decorated dislocation loops could not be detected in the Ga and Al co-implanted sample. The SIMS profiles of Al and Ga measured in the samples with and without pre-amorphization are nearly identical. Ge recrystallization has almost no effect on the distributions of the two dopants. The activation level is almost identical in both samples (4.1-4.6×10^{19} at cm^{-3}) and is very close to the maximum concentrations of both the Al and Ga SIMS profiles. However, the Ge doping level should correspond to the sum of Ga and Al distribution if the Ga and Al doses were entirely activated, suggesting that the main part of free carriers results from Ga atom activation, the concentration of activated Al atoms being negligible compared to that of Ga. As expected, Al diffusion prevented the formation of dislocation loops during annealing, allowing the activation of the entire Ga dose. However, a heat treatment with a thermal budget lower than that of the annealing R3 should be used in order to minimize Ga diffusion, allowing higher doping levels to be reached.

4. Summary and conclusion

Comparison between Ge *p*-type doping using either single Ga or Al implantation or Ga and Al co-implantation evidenced several phenomena suggesting that high *p*-type doping levels close to Ga solubility (~3-4×10^{21} cm^{-3}) can be achieved in Ge using classical CMOS processes including ion implantation and adapted rapid thermal process (RTP). Ge doping using Ga implantation is not limited by the formation of Ga clusters but by the segregation of Ga at Ge dislocation loops formed during annealing, resulting from the damages caused by Ga implantation. Indeed, high-dose Ga implantation causes Ge amorphization down to a depth of ~100 nm, with the presence of a honeycomb structure only on the first few nanometers of depth (Fig. 1). This amorphized region goes deeper than the location of the implantation peaks of both Ga and Al (~60 nm deep). It is during recrystallization of this zone that dislocation loops are formed, by diffusion and coalescence of oversaturated Ge self-interstitials [13,44,58–60]. After the formation of the dislocation loops, self-interstitial exchanges between dislocation loops, as well as between dislocation loops and the surface can take place, later after Ge recrystallization, allowing dislocation loops to coalesce and modifying dopant diffusion kinetics [60,62,63].

In the case of Ga single implantation, a part of the Ga atoms segregates on the dislocation loops limiting Ge doping level, and Ge self-interstitials do not interact with Ga diffusion, since Ga diffusion is vacancy-mediated in Ge. Indeed, Fig. S1 (see supplementary material) reports Ge self-diffusion coefficients and Ga diffusion coefficients in Ge from the literature together with the Ga diffusion coefficients determined in the present study. Data from references [28,29] were obtained using radio-tracer measurements, while the results from reference [56] were obtained using SIMS measurements on Ga-implanted samples using an energy of 150 keV. In this study, the sample preparation conditions are close to those used in our study (annealing for 3 h at 550 °C, 600 °C and 650 °C for two doses: 1×10^{15} cm^{-2} and 5×10^{13} cm^{-2}). The authors observed negligible Ga diffusion in the case of the low-dose implantation, but measured diffusion coefficients larger than those obtained in the present study in the samples implanted with the high Ga dose. These differences of diffusivity between the different studies can be explained by a difference of charge-dependent point defect concentrations due to a difference of doping levels. Similar to our observations,

the authors noted that part of the Ga atoms located in the implantation peak vicinity was immobile in high Ga dose implanted samples. The coefficients determined in the present study are in very good agreement with those measured by Sodervall et al. determined using tracer diffusion [29] and are close to that of Ge self-diffusion [64], corresponding to a diffusion mechanism mediated by Ga-vacancy pairs.

Interstitial dislocation loops are not formed during the same annealing in the case of Ga and Al co-implantation. However, the initial microstructure in the sample with a single Ga implant and in the sample co-implanted with Ga and Al is the same, with the same 100 nm-deep amorphized region due to Ga implantation, damages due to Al implantation being not detected with our experimental tools. Furthermore, the fact that dislocation loops do not form in the presence of Al is accompanied with diffusion acceleration of a fraction of the Al dose (Al concentration below 10^{18} cm^{-2} in Fig. 12). In addition, Al diffusion acceleration occurs without Ga diffusion acceleration, and the low activation level of Al atoms despite their full solubility suggests that a fraction of mobile Al atoms occupy inactive sites of the Ge lattice. All these observations suggest that Al atoms interact with Ge self-interstitials and that a fraction of them may occupy interstitial sites in Ge. However, the Al fraction showing faster diffusion with Ga implantation is not expected to use a pair mechanism between Al and Ge self-interstitial, since diffusion kinetics of elements using a pair mechanism with Ge self-interstitial, such as B, is much lower than that of Ge self-diffusion [65]. The most probable explanation is that a part of the Al atoms uses the kick-out mechanism [66]. According to this mechanism, an Al atom can exchange its substitutional site with the interstitial site of a Ge self-interstitial and diffuse rapidly on interstitial sites until exchanging sites with a substitutional Ge atom. Indeed, Ge self-interstitials are in oversaturation in Ge after the end of Ge recrystallization due to Ga implantation. Without Al, oversaturated self-interstitials gather and form interstitial dislocation loops. However, if Al is present in the sample, substitutional Al atoms can exchange positions with self-interstitials (i.e. kick-out mechanism) preventing dislocation loop formation and diffuse rapidly deeper in the Ge crystal, independently of vacancy-mediated Ga diffusion.

Thus, high *p*-type doping levels should be reached in Ge using the appropriate process following: i) Ga and Al co-implantation, ii) RTP pre-annealing, such as the annealing R0, allowing a large part of implantation-mediated defects to be cured without significant dopant diffusion, and iii) second RTP annealing with a thermal budget lower than that of the annealing R3, allowing the entire Ga dose to be activated without dislocation loop formation and without significant Ga diffusion, to get high doping levels.

CRediT authorship contribution statement

J. Perrin Toinin: Writing – original draft, Visualization, Validation, Investigation, Formal analysis, Data curation. **A. Portavoce:** Writing – review & editing, Writing – original draft, Supervision, Project administration, Methodology, Funding acquisition, Conceptualization. **M. Bertoglio:** Methodology, Investigation. **M. Descoins:** Methodology, Investigation. **M. Texier:** Validation, Investigation. **D. Narducci:** Validation, Investigation. **R. Daineche:** Investigation. **K. Hoummada:** Writing – review & editing, Supervision, Methodology, Conceptualization.

Declaration of competing interest

The authors declare that they have no known competing financial interests or personal relationships that could have appeared to influence the work reported in this paper.

Acknowledgements

This work was supported by the French National Agency for Research (ANR) through the program “Science de l’ingénierie” (Project DoGeTec, no. ANR-12-JS09-0015-1).

Appendix A. Supplementary data

Supplementary data to this article can be found online at https://doi.org/10.1016/j.mssp.2025.109877.

Data availability

All the necessary data is available in the main text. Any other relevant data are also available upon request.

References

[1] T. Skotnicki, J.A. Hutchby, T.-J. King, H.-S.P. Wong, F. Boeuf, The end of CMOS scaling: toward the introduction of new materials and structural changes to improve MOSFET performance, IEEE Circ. Dev. Mag. 21 (2005) 16–26, https://doi.org/10.1109/mcd.2005.1388765.
[2] C.H. Fu, Y.H. Lin, W.C. Lee, T.D. Lin, R.L. Chu, L.K. Chu, P. Chang, M.H. Chen, W. J. Hsueh, S.H. Chen, G.J. Brown, J.I. Chyi, J. Kwo, M. Hong, Self-aligned inversion-channel n-InGaAs, p-GaSb, and p-Ge MOSFETs with a common high j gate dielectric using a CMOS compatible process, Microelec, Eng. 147 (2015) 330–334.
[3] B. Vincent, J.F. Damlencourt, Y. Morand, A. Pouydebasque, C. Le Royer, L. Clavelier, N. Dechoux, P. Rivallin, T. Nguyen, S. Cristoloveanu, Y. Campidelli, D. Rouchon, M. Mermoux, S. Deleonibus, D. Bensahel, T. Billon, The Ge condensation technique: a solution for planar SOI/GeOI co-integration for advanced CMOS technologies? Mater. Sci. Semicond. Process. 11 (2008) 205–213.
[4] Z. Zhou, B. Yin, J. Michel, On-chip light sources for silicon photonics, Light Sci. Appl. 4 (2015) e358.
[5] M. Bouabdellaoui, M. Bollani, M. Salvalaglio, E. Assaf, L. Favre, M. Abel, A. Ronda, O. Gourhant, F. Deprat, C. Duluard, A.-F. Mallet, P. Vennegues, J.-N. Aqua, I. Berbezier, Engineering epitaxy and condensation: fabrication of Ge nanolayers, mechanism and applications, Appl. Surf. Sci. 630 (2023) 157226.
[6] Physics of Semiconductor Devices | Wiley Online Books, (n.d.). https://onlinelibrary.wiley.com/doi/book/10.1002/0470068329 (accessed August 9, 2022).
[7] R. Skrotzki, T. Herrmannsdörfer, V. Heera, J. Fiedler, A. Mücklich, M. Helm, J. Wosnitza, The impact of heavy Ga doping on superconductivity in germanium, Low Temp. Phys. 37 (2011) 877–883, https://doi.org/10.1063/1.3671590.
[8] S. Prucnal, V. Heera, R. Hübner, M. Wang, G.P. Mazur, M.J. Grzybowski, X. Qin, Y. Yuan, M. Voelskow, W. Skorupa, L. Rebohle, M. Helm, M. Sawicki, S. Zhou, Superconductivity in single-crystalline aluminum- and gallium-hyperdoped germanium, Phys. Rev. Mater. 3 (2019) 054802, https://doi.org/10.1103/PhysRevMaterials.3.054802.
[9] D.C. Mueller, W. Fichtner, Codoping as a measure against donor deactivation in Si: ab initio calculations, Phys. Rev. B 73 (2006) 035210, https://doi.org/10.1103/PhysRevB.73.035210.
[10] J. Kim, S.W. Bedell, S.L. Maurer, R. Loesing, D.K. Sadana, Activation of implanted n-Type dopants in Ge over the active concentration of 1×10^{20} cm^{-3} using coimplantation of Sb and P, Electrochem. Solid State Lett. 13 (2010) H12–H15, https://doi.org/10.1149/1.3257912.
[11] D. Pastor, H.H. Gandhi, C.P. Monmeyran, A.J. Akey, R. Milazzo, Y. Cai, E. Napolitani, R.M. Gwilliam, I.F. Crowe, J. Michel, L.C. Kimerling, A. Agarwal, E. Mazur, M.J. Aziz, High level active n+ doping of strained germanium through co-implantation and nanosecond pulsed laser melting, J. Appl. Phys. 123 (2018) 165101, https://doi.org/10.1063/1.5012512.
[12] W.L. Brown, R.G. Elliman, R.V. Knoell, A. Leiberich, J. Linnros, D.M. Maher, J. S. Williams, Interfacial crystallization and amorphization of silicon under ion bombardment, in: Microsc. Semicond. Mater. 1987, CRC Press, 1987.
[13] A. Claverie, S. Koffel, N. Cherkashin, G. Benassayag, P. Scheiblin, Amorphization, recrystallization and end of range defects in germanium, Thin Solid Films 518 (2010) 2307–2313, https://doi.org/10.1016/j.tsf.2009.09.162.
[14] I.H. Wilson, The effects of self-ion bombardment (30–500 keV) on the surface topography of single-crystal germanium, J. Appl. Phys. 53 (1982) 1698–1705, https://doi.org/10.1063/1.331636.
[15] L.M. Wang, R.C. Birtcher, Radiation-induced formation of cavities in amorphous germanium, Appl. Phys. Lett. 55 (1989) 2494–2496, https://doi.org/10.1063/1.102009.
[16] B. Stritzker, R.G. Elliman, J. Zou, Self-ion-induced swelling of germanium, Nucl. Instrum. Methods Phys. Res. Sect. B Beam Interact. Mater. At. 175–177 (2001) 193–196, https://doi.org/10.1016/S0168-583X(00)00597-8.
[17] L.M. Wang, R.C. Birtcher, Amorphization, morphological instability and crystallization of Krypton ion irradiated germanium, Philos. Mag. A 64 (1991) 1209–1223, https://doi.org/10.1080/01418619108225344.
[18] O.W. Holland, B.R. Appleton, J. Narayan, Ion implantation damage and annealing in germanium, J. Appl. Phys. 54 (1983) 2295–2301, https://doi.org/10.1063/1.332385.
[19] L. Ottaviano, A. Verna, V. Grossi, P. Parisse, S. Piperno, M. Passacantando, G. Impellizzeri, F. Priolo, Surface morphology of Mn+ implanted Ge(100): a systematic investigation as a function of the implantation substrate temperature, Surf. Sci. 601 (2007) 2623–2627, https://doi.org/10.1016/j.susc.2006.11.075.

[20] L. Romano, G. Impellizzeri, M.V. Tomasello, F. Giannazzo, C. Spinella, M. G. Grimaldi, Nanostructuring in Ge by self-ion implantation, J. Appl. Phys. 107 (2010) 084314, https://doi.org/10.1063/1.3372757.
[21] T. Janssens, C. Huyghebaert, D. Vanhaeren, G. Winderickx, A. Satta, M. Meuris, W. Vandervorst, Heavy ion implantation in Ge: dramatic radiation induced morphology in Ge, J. Vac. Sci. Technol., B: Microelectron. Nanometer Struct.–Process., Meas., Phenom. 24 (2006) 510–514, https://doi.org/10.1116/1.2151904.
[22] L. Romano, G. Impellizzeri, L. Bosco, F. Ruffino, M. Miritello, M.G. Grimaldi, Nanoporosity induced by ion implantation in deposited amorphous Ge thin films, J. Appl. Phys. 111 (2012) 113515, https://doi.org/10.1063/1.4725427.
[23] B.L. Darby, B.R. Yates, N.G. Rudawski, K.S. Jones, A. Kontos, R.G. Elliman, Insights for void formation in ion-implanted Ge, Thin Solid Films 519 (2011) 5962–5965, https://doi.org/10.1016/j.tsf.2011.03.040.
[24] F.A. Trumbore, E.M. Porbansky, A.A. Tartaglia, Solid solubilities of aluminum and gallium in germanium, J. Phys. Chem. Solid. 11 (1959) 239–245, https://doi.org/10.1016/0022-3697(59)90220-3.
[25] W. Meer, D. Pommerrenig, Diffusion von Aluminium und Bor in Germanium, Z. Angew. Phys. 23 (1967) 369–372.
[26] W. Gust, A. Lodding, H. Odelius, B. Predel, U. Roll, P. Dorner, Sims-untersuchungen zur volumendiffusion von Al in Ge, Acta Metall. 30 (1982) 941–946, https://doi.org/10.1016/0001-6160(82)90200-0.
[27] J. Räisänen, Annealing behaviour of aluminium implanted germanium, Solid State Electron. 25 (1982) 49–54, https://doi.org/10.1016/0038-1101(82)90093-4.
[28] W.C. Dunlop, Diffusion of impurities in germanium, Phys. Rev. 94 (1954) 1531–1540, https://doi.org/10.1103/PhysRev.94.1531.
[29] U. Södervall, H. Odelius, A. Lodding, U. Roll, B. Predel, W. Gust, P. Dorners, Gallium tracer diffusion and its isotope effect in germanium, Philos. Mag. A 54 (1986) 539–551, https://doi.org/10.1080/01418618608243611.
[30] A.L. Demirel, S. Strite, A. Agarwal, M.S. Ünlü, H. Morkoç, A. Rockett, Reduction of outdiffusion at the Ge/GaAs (100) interface by low temperature growth, J. Vac. Sci. Technol., B: Microelectron. Nanometer Struct.–Process., Meas., Phenom. 10 (1992) 664–667, https://doi.org/10.1116/1.586429.
[31] K. Schmid, H. Kranz, H. Ryssel, , et al.W. Muller, Phys. Status Solidi 23 (1974) 1523.
[32] S. Mirabella, G. Impellizzeri, A. Piro, E. bruno, , et al.M. Grimaldi, Appl. Phys. Lett. 92 (2008) 251909.
[33] G. Impellizzeri, S. Mirabella, A. Irrera, M.G. Grimaldi, E. Napolitani, Ga-implantation in Ge: electrical activation and clustering, J. Appl. Phys. 106 (2009) 1013518, https://doi.org/10.1063/1.3159031.
[34] H. Bracht, S. Schneider, R. Kube, Diffusion and doping issues in germanium, Microelectron. Eng. 88 (2011) 452–457, https://doi.org/10.1016/j.mee.2010.10.013.
[35] J.F. Ziegler, M.D. Ziegler, J.P. Biersack, SRIM – the stopping and range of ions in matter (2010), Nucl. Instrum. Methods Phys. Res. Sect. B Beam Interact. Mater. At. 268 (2010) 1818–1823, https://doi.org/10.1016/j.nimb.2010.02.091.
[36] M.K. Miller, K.F. Russell, K. Thompson, R. Alvis, D.J. Larson, Review of Atom probe FIB-Based specimen preparation methods, Microsc. Microanal. 13 (2007) 428–436, https://doi.org/10.1017/S1431927607070845.
[37] S. Koffel, P. Scheiblin, A. Claverie, G. Benassayag, Amorphization kinetics of germanium during ion implantation, J. Appl. Phys. 105 (2009) 1013528, https://doi.org/10.1063/1.3041653.
[38] R. Sielemanna, H.H. asslein, C. Zistl, M. Muller, L. Stadler, V. Emtsev, Physica B 308–310 (2001) 529.
[39] J. Perrin Toinin, A. Portavoce, M. Texier, M. Bertoglio, K. Hoummada, Te homogeneous precipitation in Ge dislocation loop vicinity, Appl. Phys. Lett. 108 (2016) 232103, https://doi.org/10.1063/1.4953627.
[40] S. Fischler, J. Appl. Phys. 33 (1962) 11615.
[41] L. Hutin, S. Koffel, C. Le Royer, L. Clavelier, P. Scheiblin, V. Mazzocchi, , et al. S. Deleonibus, Mater. Sci. Semicond. Process. 11 (2008) 267.
[42] T. Luo, J. Perrin Toinin, M. Descoins, K. Hoummada, M. Bertoglio, L. Chow, D. Narducci, A. Portavoce, PdGe contact fabrication on Ga-doped Ge: influence of implantation-mediated defects, Scr. Mater. 150 (2018) 66–69, https://doi.org/10.1016/j.scriptamat.2018.02.037.
[43] A. Portavoce, N. Rodriguez, R. Daineche, C. Grosjean, C. Girardeaux, Correction of secondary ion mass spectrometry profiles for atom diffusion measurements, Mat, Letture 63 (2009) 676–678, https://doi.org/10.1016/j.matlet.2008.12.018.
[44] A. De Luca, A. Portavoce, M. Texier, C. Grosjean, N. Burle, V. Oison, B. Pichaud, Tungsten diffusion in silicon, J. Appl. Phys. 115 (2014) 013501, https://doi.org/10.1063/1.4859455.
[45] Collaboration: authors and editors of the volumes III/22b-41A2a, Germanium (Ge), solubility of impurities, general, in: O. Madelung, U. Rössler, M. Schulz (Eds.), Impurities Defects Group IV Elem. IV-IV III-V Compd. Part Group IV Elem, Springer-Verlag, Berlin/Heidelberg, 2002, pp. 1–3, https://doi.org/10.1007/10681604_143.
[46] K. Hoummada, D. Mangelinck, B. Gault, M. Cabié, Nickel segregation on dislocation loops in implanted silicon, Scr. Mater. 64 (2011) 378–381, https://doi.org/10.1016/j.scriptamat.2010.10.036.
[47] A. Portavoce, G. Tréglia, Theoretical investigation of Cottrell atmosphere in silicon, Acta Mater. 65 (2014) 1–9, https://doi.org/10.1016/j.actamat.2013.11.053.
[48] M.K. Miller, Atome Probe Tomography: Analysis at the Atomic Level, Kluwer Academic/Plenum Publisher, New York, 2000, p. 152, chap. 5.
[49] P. Maugis, K. Hoummada, A methodology for the measurement of the interfacial excess of solute at a grain boundary, Scr. Mater. 120 (2016) 90–93, https://doi.org/10.1016/j.scriptamat.2016.04.005.
[50] Atom-Probe tomography, n.d. https://link.springer.com/book/10.1007/978-1-4899-7430-3. (Accessed 20 July 2022).
[51] A. Giese, H. Bracht, N. Stolwijk, H. Mehrer, Diffusion of nickel and zinc in germanium, defect Diffus, Forum 143–147 (1997) 1059–1066. https://doi.org/10.4028/www.scientific.net/DDF.143-147.1059.
[52] A. Portavoce, O. Abbes, Y. Rudzevich, L. Chow, V. Le Thanh, C. Girardeaux, Manganese diffusion in monocrystalline germanium, Scr. Mater. 67 (2012) 269–272, https://doi.org/10.1016/j.scriptamat.2012.04.038.
[53] A. Portavoce, Anomalous B diffusion profiles in nanocrystalline Si, Scr. Mater. 99 (2015) 37–40, https://doi.org/10.1016/j.scriptamat.2014.11.021.
[54] F.J. Morin, Lattice-Scattering mobility in germanium, Phys. Rev. 93 (1954) 62–63, https://doi.org/10.1103/PhysRev.93.62.
[55] P. Rai Choudhury, F.A. Selim, W.J. Takei, Diffusion and incorporation of aluminum in silicon, J. Electrochem. Soc. 124 (1977) 762, https://doi.org/10.1149/1.2133402.
[56] N. Ioannou, D. Skarlatos, N.Z. Vouroutzis, S.N. Georga, C.A. Krontiras, C. Tsamis, Gallium implantation and diffusion in crystalline germanium, Electrochem. Solid State Lett. 13 (2009) H70, https://doi.org/10.1149/1.3274801.
[57] A. De Luca, A. Portavoce, M. Texier, C. Grosjean, N. Burle, V. Oison, B. Pichaud, Tungsten diffusion in silicon, J. Appl. Phys. 115 (2014) 013501, https://doi.org/10.1063/1.4859455.
[58] F. Cristiano, J. Grisolia, B. Colombeau, M. Omri, B. de Mauduit, A. Claverie, L. F. Giles, N.E.B. Cowern, Formation energies and relative stability of perfect and faulted dislocation loops in silicon, J. Appl. Phys. 87 (2000) 8420–8428, https://doi.org/10.1063/1.373557.
[59] F. Cristiano, N. Cherkashin, X. Hebras, P. Calvo, Y. Lamrani, E. Scheid, B. de Mauduit, B. Colombeau, W. Lerch, S. Paul, A. Claverie, Ion beam induced defects in crystalline silicon, Nucl. Instrum. Methods Phys. Res. Sect. B Beam Interact. Mater. At. 216 (2004) 46–56, https://doi.org/10.1016/j.nimb.2003.11.019.
[60] S. Boninelli, N. Cherkashin, A. Claverie, F. Cristiano, Transformation of {113} defects into dislocation loops mediated by the {111} rod-like defects, Nucl. Instrum. Methods Phys. Res. Sect. B Beam Interact. Mater. At. 253 (2006) 80–84, https://doi.org/10.1016/j.nimb.2006.10.019.
[61] P. Delugas, V. Fiorentini, Energetics of transient enhanced diffusion of boron in Ge and SiGe, Phys. Rev. B 69 (2004) 085203, https://doi.org/10.1103/PhysRevB.69.085203.
[62] A. Claverie, B. Colombeau, G. Ben Assayag, C. Bonafos, F. Cristiano, M. Omri, B. de Mauduit, Thermal evolution of extended defects in implanted Si: impact on dopant diffusion, Mater. Sci. Semicond. Process. 3 (2000) 269–277, https://doi.org/10.1016/S1369-8001(00)00043-3.
[63] A. Claverie, B. Colombeau, F. Cristiano, A. Altibelli, C. Bonafos, Modeling of the Ostwald ripening of extrinsic defects and transient enhanced diffusion in silicon, Nucl. Instrum. Methods Phys. Res. Sect. B Beam Interact. Mater. At. 186 (2002) 281–286, https://doi.org/10.1016/S0168-583X(01)00914-4.
[64] M. Werner, H. Mehrer, H.D. Hochheimer, Effect of hydrostatic pressure, temperature, and doping on self-diffusion in germanium, Phys. Rev. B 32 (1985) 3930–3937, https://doi.org/10.1103/PhysRevB.32.3930.
[65] S. Mirabella, D. De Salvador, E. Napolitani, E. Bruno, F. Priolo, Mechanisms of boron diffusion in silicon and germanium, J. Appl. Phys. 113 (2013) 031101, https://doi.org/10.1063/1.4763353.
[66] P. Pichler, Intrinsic Point Defects, Impurities, and Their Diffusion in Silicon, 3, Springer-Verlag, Wien, 2004, p. 272.